MITSUBISHI ELECTRIC RESEARCH LABORATORIES
https://www.merl.com

Lunar Landing with Feasible Divert using Controllable Sets

Srinivas, Neeraj; Vinod, Abraham P.; Di Cairano, Stefano; Weiss, Avishai

TR2024-004 January 09, 2024

Abstract

We develop a guidance policy for a lunar lander under state and input constraints to land at a nominal target location, while maintaining the ability to divert to alternative landing sites if a hazard is detected. To ensure divert feasibility, we compute controllable sets that characterize the set of states that can be driven to a landing site for a range of fuel mass and length of divert trajectories. In the event a hazard is detected, we select the best divert feasible set among the landing targets according to a scoring metric of attributes such as fuel utilization and hazards. Simulations of the policy demonstrate that the lander can safely divert to an alternative landing site after a hazard is detected. We develop a visualization environment using Unreal Engine to render a landing trajectory at the lunar south pole using high fidelity digital elevation maps obtained by the Lunar Reconnaissance Orbiter. The visualization environment enables us to generate synthetic imagery of the lunar surface for terrain relative navigation and hazard detection.

AIAA SciTech 2024

Mitsubishi Electric Research Laboratories, Inc.
201 Broadway, Cambridge, Massachusetts 02139

Lunar Landing with Feasible Divert using Controllable Sets

Neeraj Srinivas*
Virginia Polytechnic Institute and State University, Blacskburg, VA, 24060

Abraham P. Vinod,† Stefano Di Cairano,‡ and Avishai Weiss §
Mitsubishi Electric Research Laboratories, Cambridge, MA, 02139

We develop a guidance policy for a lunar lander under state and input constraints to land at a nominal target location, while maintaining the ability to divert to alternative landing sites if a hazard is detected. To ensure divert feasibility, we compute controllable sets that characterize the set of states that can be driven to a landing site for a range of fuel mass and length of divert trajectories. In the event a hazard is detected, we select the best divert feasible set among the landing targets according to a scoring metric of attributes such as fuel utilization and hazards. Simulations of the policy demonstrate that the lander can safely divert to an alternative landing site after a hazard is detected. We develop a visualization environment using Unreal Engine to render a landing trajectory at the lunar south pole using high fidelity digital elevation maps obtained by the Lunar Reconnaissance Orbiter. The visualization environment enables us to generate synthetic imagery of the lunar surface for terrain relative navigation and hazard detection.

I. Introduction

As lunar exploration sees a resurgence of activity, and a permanent human presence on the Moon gets closer to reality, the ability to land at specific areas of interest on the lunar surface are of paramount importance. With increasing attention focused on the water ice located at the south pole of the Moon [1], this work presents an integrated study on achieving soft landings at points of interest, while maintaining the feasibility to divert to alternative landing sites if a hazard is detected.

Numerous space agencies such as NASA [2], JAXA [3], and ISRO [4], as well as private enterprises such as iSPACE [5] aim to further explore the lunar surface using landers and rovers. Due in part to this renewed activity and interest in lunar exploration, a number of studies have been conducted in recent years to achieve autonomous guidance, navigation, and control for lunar landings. Although the Apollo missions successfully utilized a polynomial guidance law for powered-descent, and manual control of the spacecraft for the terminal descent phase, these trajectories were not propellant-optimal, and had landing uncertainty ellipses on the scale of kilometers [6, 7]. To overcome these drawbacks, the NASA Autonomous Landing and Hazard Avoidance Technology (ALHAT) [8] program has been deployed since 2008 to detect hazards and perform divert maneuvers at the approach and terminal descent phases (at altitudes of 1-2 kilometers and 30 meters, respectively), with landing ellipses on the order of tens of meters. Recent advances in technology have enabled a more robust autonomous approach to precision landings. Utilization of terrain relative navigation (TRN) techniques has enabled more accurate state estimation in planetary and lunar landing problems, and was incorporated in the Mars 2020 mission [9]. Real-time implementation of powered descent guidance (PDG) algorithms have been facilitated by the development of computationally efficient interior-point algorithms [10]. Finally, guidance and control algorithms that incorporate vision-based data have been developed for pin-point landing accuracy, for example as utilized in the JAXA SLIM mission [11].

Diverting from the initially intended landing site may be necessary due to, for example, hazard detection, crater impacts, and the a priori unavailability of high quality terrain data. Ho et al. discuss deep-learning methods for safe landing site selection, with considerations for divert maneuvers in [12]. Model predictive control (MPC) based methods for soft landing have been proposed in [13, 14], which have the ability to incorporate algorithms for diverts [15].

*Graduate Student (neeraj21@vt.edu), Kevin T. Crofton department of Aerospace and Ocean Engineering. N. Srinivas interned at MERL during the development of this work.

†Research Scientist (vinod@merl.com)

‡Distinguished Research Scientist (dicairano@merl.com)

§Senior Principal Research Scientist (weiss@merl.com)

In this work, we utilize the convex optimization-based minimum-fuel PDG algorithm [16] to develop fuel-optimal trajectories, and based on the work in [17], compute the set of initial conditions from which landing at a specific target can be achieved. Trajectories from these initial conditions are guaranteed to reach the designated target landing spot, while satisfying all state and path constraints. These controllable sets are generated for a range of divert lengths and fuel mass values, to facilitate divert capabilities at various points along the final descent stage. A trajectory generation algorithm is then developed to divert-feasible landing sites, incorporating factors such as fuel utilization and hazards at the site to dynamically change the order of priority of the divert lading sites. The algorithm selects the best divert feasible set from the pre-computed controllable sets that facilitates landing at the selected alternate landing site. The 3D computer graphics game engine Unreal Engine 4.26 is utilized in conjunction with Simulink to develop a high-fidelity environment of the lunar south pole region, where the computed trajectories are visualized. The visualization environment enables the implementation of real-time state estimation based on topographic digital elevation data and computer vision algorithms and allows us to simulate hazards at the primary landing site, which are detected via a LiDAR sensor.

The rest of this paper is structured as follows. Section II introduces the lander dynamics, constraints, and the powered descent guidance problem. In section III we describe controllable sets and their use to compute divert-feasible states. Section IV develops the algorithm for trajectory generation with feasible divert. In section V we present simulation results for nominal and divert trajectories after a hazard is detected. In section VI we describe the environment developed using Unreal Engine to visualize landing trajectories for terrain relative navigation and demonstration of hazard detection on the primary landing site. Finally, we discuss future work and provide concluding remarks in section VII.

Notation: The interval $\mathbb{N}_{[a,b]}$ enumerates all natural numbers between and including $a, b \in \mathbb{N}$. Euclidean distance is denoted by $\|\cdot\|$. Given a continuous time signal $x(t)$ sampled with period ΔT, we denote the value at time instant $k\Delta T$, $k \in \mathbb{N}$, by $x_k = x(k\Delta T)$.

II. Problem Formulation & Preliminaries

In this section we describe the lander dynamics model, state and input constraints, the powered descent guidance problem, and define the problem statement.

A. Lander Dynamics and Constraints

Consider the 3 degrees of freedom (3-DOF) dynamics model of the lunar lander,

$$\dot{r} = v, \tag{1a}$$

$$\dot{v} = \frac{u}{m} + g_{\text{moon}}, \tag{1b}$$

$$\dot{m} = -\frac{\|u\|_2}{g_{\text{earth}} I_{\text{sp}}}, \tag{1c}$$

with position $r = [r_1, r_2, r_3] \in \mathbb{R}^3$, velocity $v = [v_1, v_2, v_3] \in \mathbb{R}^3$, mass of the spacecraft $m \geq m_{\text{dry}}$, where $m_{\text{dry}} > 0$ is the mass of the lander without any fuel, thrust $u \in \mathbb{R}^3$, gravity with respect to earth $g_{\text{earth}} = -9.81 m/s^2$, gravity vector with respect to the moon $g_{\text{moon}} = [0; 0; -1.62]^T m/s^2$, and the specific impulse of the engine I_{sp}. We ignore the effects of planetary rotation and consider a constant gravity model. We can represent (1) compactly with the nonlinear, continuous-time dynamics,

$$\dot{x} = f(x, u), \tag{2}$$

where $x = [r, v, m] \in \mathbb{R}^7$.

The thrust u is subject to the constraint $u \in \mathcal{U}$, where the input set $\mathcal{U}$ is given by

$$\mathcal{U} = \{u : 0 < \rho_{\text{lower}} \leq \|u\| \leq \rho_{\text{upper}},\ \hat{n}^\top u \geq \|u\| \cos(\theta)\}. \tag{3}$$

The input set $\mathcal{U}$ requires that the thrust is bounded from above and below with known constants $\rho_{\text{lower}}, \rho_{\text{upper}}$, and requires the attitude constraint that the deviation angle between the thrust u and a pre-specified unit vector $\hat{n} \in \mathbb{R}^3$ be less than a pre-specified bound $\theta \in [0, \pi]$.

The lander trajectory is constrained to be contained within a feasible cone with a pre-specified landing target with the minimum glide slope angle γ_{gs} specified by

$$\mathcal{X} = \left\{ x \in \mathbb{R}^7 : \tan(\gamma_{\text{gs}}) \leq \frac{r_3}{\sqrt{r_1^2 + r_2^2}} \right\}. \tag{4}$$

B. Powered Descent Guidance using Convex Optimization

We adopt the minimum-fuel powered descent guidance (PDG) framework [16, 18]. Specifically, we design a thrust profile $u(t) \in \mathcal{U}$ which, when applied to the spacecraft, takes it from a pre-specified initial state $x(0)$ to rest at the origin in minimum time $t_f > 0$ with non-negative terminal mass $m(t_f) > 0$.

We formulate the lunar landing problem as the solution of the following continuous-time optimization problem,

$$\begin{aligned} \underset{t_f, u(\cdot)}{\text{minimize}} \quad & -m(t_f) \\ \text{subject to} \quad & \dot{x} = f(x,u), \qquad \forall t \in [0, t_f], \\ & u(t) \in \mathcal{U},\ x(t) \in \mathcal{X}, \qquad \forall t \in [0, t_f], \\ & r(0) = r_0,\ v(0) = v_0,\ m(0) = m_{\text{dry}} + m_{\text{fuel}}, \\ & r(t_f) = 0,\ v(t_f) = 0,\ m(t_f) > m_{\text{dry}}. \end{aligned} \tag{5}$$

Problem (5) is a nonconvex due to the nonlinear dynamics (1) and the lower bound on the thrust magnitude ρ_{lower} and thus difficult to solve. In [16], it was shown that the change of variables $z = ln(m)$, $\bar{u} = u/m$, $\sigma = ||u||/m$, and a "lossless" convex relaxation of the constraints in (5) yields an optimization problem whose solution is the optimizer of (5). For tractability, [16] proposes a first-order hold of the continuous-time dynamics (2) at time steps $t_k = k\Delta t$ for some discrete-time step Δt to arrive at a discrete-time model,

$$\underbrace{\begin{bmatrix} r_{k+1} \\ v_{k+1} \\ z_{k+1} \end{bmatrix}}_{\xi_{k+1}} = \underbrace{\begin{bmatrix} r_k + \frac{\Delta t}{2}(v_k + v_{k+1}) + \frac{\Delta t^2}{12}(\bar{u}_{k+1} - \bar{u}_k) \\ v_k + \frac{\Delta t}{2}(\bar{u}_k + \bar{u}_{k+1}) + g\Delta t \\ z_k - \frac{\alpha \Delta t}{2}(\sigma_k + \sigma_{k+1}) \end{bmatrix}}_{F_{\Delta t}(\xi_k, \mu_k)} \tag{6}$$

with state $\xi = [r, v, z] \in \mathbb{R}^7$ and input $\mu = [\bar{u}, \sigma] \in \mathbb{R}^4$. Using (6), [16] proposes the second-order cone program (SOCP) for a given time of flight $t_f > 0$, control horizon $N \in \mathbb{N}$, initial mass $m(0)$, and initial state $\xi_0 = [r_0, v_0, \ln(m(0))]$,

$$\begin{aligned} \underset{\mu_0, \ldots, \mu_{N-1}}{\text{minimize}} \quad & -z_N \\ \text{subject to} \quad & r_N = v_N = 0, \\ \forall k \in \mathbb{N}_{[0,N-1]}, \quad & \xi_{k+1} = F_{\Delta t}(\xi_k, \mu_k), \\ \forall k \in \mathbb{N}_{[0,N-1]}, \quad & ||\bar{u}_k|| \leq \sigma_k, \\ \forall k \in \mathbb{N}_{[0,N-1]}, \quad & \rho_{\text{lower}} e^{-\eta_k}[1 - (z_k - \eta_k) + \tfrac{(z_k - \eta_k)^2}{2}] \leq \sigma_k \leq \rho_{\text{upper}} e^{-\eta_k}[1 - (z_k - \eta_k)], \\ \forall k \in \mathbb{N}_{[0,N-1]}, \quad & \eta_k \leq z_k \leq \ln(m(0) - \alpha \rho_{\text{lower}} k \Delta t), \\ \forall k \in \mathbb{N}_{[0,N-1]}, \quad & \bar{u}_{3,k} \geq \cos(\theta)\sigma_k, \\ \forall k \in \mathbb{N}_{[1,N]}, \quad & ||(r_{1,k}, r_{2,k})|| \tan(\gamma_{\text{gs}}) \leq r_{3,k}, \end{aligned} \tag{7}$$

where $\Delta t = t_f/N$ and $\eta_k = \ln(m(0) - \alpha \rho_{\text{upper}} k \Delta t)$ for $k \in \{0, \ldots, N-1\}$ is a collection of pre-defined constants. This formulation of the PDG problem can be solved in polynomial time and has been demonstrated to work in real-time applications [19].

Problem (7) depends on the time of flight t_f, which determines discrete-time step size Δ and the amount of fuel at landing $m(t_f) = \exp(z_N)$. We ensure minimum fuel usage by optimizing time of flight t_f. As done in [18], a golden search algorithm repeatedly solves (7) in order to compute the optimal time of flight value t_f.

C. Problem Statement

Problem 1 *Given an initial state and constraints on the thrust and glide slope of the lander, design a trajectory for the lander to successfully land at a pre-specified target location, while maintaining the ability to divert to alternative target locations in the event a hazard is detected.*

III. Controllable and Divert-Feasible Sets

A. Characterization of Divert-Feasible States

We next characterize the set of states ξ_0 from which we can divert to a prescribed landing site $\ell = [\ell_1, \ell_2, 0] \in \mathbb{R}^3$. First, we use the k-step controllable set [20] to characterize the states that can be driven to $\ell = 0$ in k steps while satisfying thrust and glide slope constraints for some fixed $\Delta t'$ (possibly different from Δt used in (6)),

$$\mathcal{K}(m, D) = \{\xi_0 \in \mathbb{R}^7 | \forall k \in \mathbb{N}_{[0,D-1]}, \exists \mu_k \in \mathbb{R}^4, \xi_{k+1} = F_{\Delta t'}(\xi_k, \mu_k) \text{ such that constraints in (7) are satisfied}\}, \quad (8)$$

for any mass before divert $m > 0$ and any length of divert trajectory $D \in \mathbb{N}$. For a landing site $\ell \neq 0$, we can translate the set $\mathcal{K}$ by $-\ell$, which corresponds to the k-step controllable set in a new coordinate frame where the landing site is at the origin. Thus, the set of divert-feasible states $\mathcal{B}(\ell; m, D)$ for any landing site ℓ is given by the Minkowski sum of $\mathcal{K}(m, D)$ and $\{-\ell\}$,

$$\mathcal{B}(\ell; m, D) = \mathcal{K}(m, D) \oplus \{-\ell\}. \quad (9)$$

B. Computation of controllability sets

A convex optimization based method introduced in [17] is adopted in this work to calculate the set of initial conditions from which the target can be reached, subject to all dynamics and constraints as described in problem (7). Solutions of the optimization problem (7) to alternate landing sites are dependent on the mass of fuel $m(0)$ available at the start of the divert maneuver and the length of divert trajectory D. The divert length D and initial mass $m(0)$ are treated as independent variables that determine the solution of (7). By setting the objective function in (7) to be $\mathbf{a}_j \boldsymbol{\eta}$, where $\mathbf{a}_j$ is a set of unit vectors $\pm\mathbf{e}_j$, $j = 1, 2, \ldots n$, and $\boldsymbol{\eta}$ is the vector of initial conditions $x_0 = [r_x(0); r_y(0); r_z(0); v_x(0); v_y(0); v_z(0)]^T$, trajectories are generated such that each initial condition $\mathbf{a}_j \boldsymbol{\eta}$ is maximized, resulting in a set of 6 dimensional states that correspond to the greatest initial conditions such that the target is reached. Taking the convex hull of the set of initial conditions constructs a preliminary constrained controllability set of initial states from which the target is guaranteed to be reached, for a given amount of mass of fuel $m(0)$ and a given divert length D. Further details of the polytope generation algorithm can be found in [17].

An example controllability set is represented in Figure 1, with projections onto the position and velocity coordinates. Custom solvers have demonstrated the constrained controllability sets can be computed with low computational times [19], allowing for a large number of the constrained controllability polytopes to be constructed. This work assumes a large number of polytopes are constructed prior to launch and stored onboard the lander.

A 2 dimensional array of controllable sets is constructed, corresponding to various fuel mass and divert length values $[m(0) + n\Delta m(0), D + p\Delta D]$ respectively, for a total of np sets. Table 1 depicts projections of a subset of the 2-D array of controllable sets onto the position dimensions, with mass dimensions along the x-axis and divert lengths along the y-axis. It can be observed that the sets corresponding to various D values vary more in dimensions from one another, as time of flight restricts the maximum fuel available to be used.

IV. Trajectory Generation and Divert Landing Site Selection

A few factors have to be taken into account for landing site selection. It is assumed in this work that a primary target zone has been chosen as part of the mission design. For example, a comparatively flat area of 1 km × 1 km is selected as the overall target zone, near the lunar south pole. The guidance algorithm must now determine the optimal landing zone within this primary region. Three factors have been chosen in this work to weigh the decision. Every landing site identified within the primary region is assigned the following attributes :

- **Cost of reachability:** The mass of fuel required to reach the landing site. A landing site that requires a lower amount of fuel to reach is given a higher priority, as this ensures greater fuel availability in case of a second divert requirement.

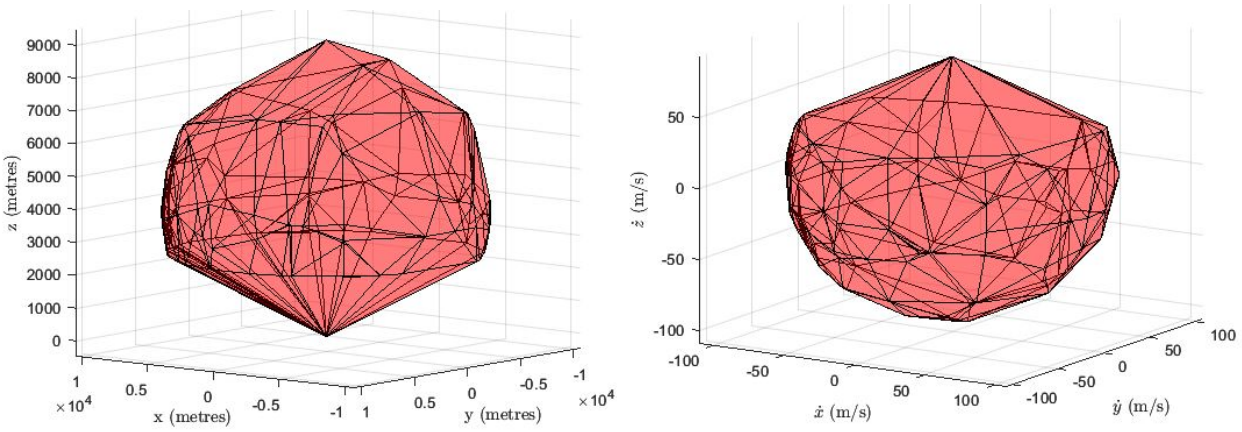

(a) Projection of $\mathcal{K}$ on position coordinates **(b) Projection of $\mathcal{K}$ on velocity coordinates**

Fig. 1 Example D-step controllable set $\mathcal{K}$ projections onto position and velocity coordinates

	$m = 1780\ kg$	$m = 1800\ kg$	$m = 1820\ kg$
$D = 20$	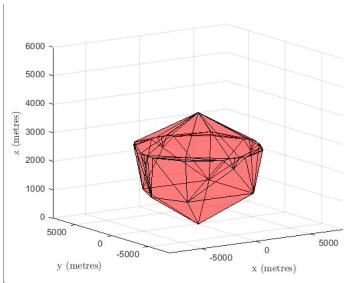	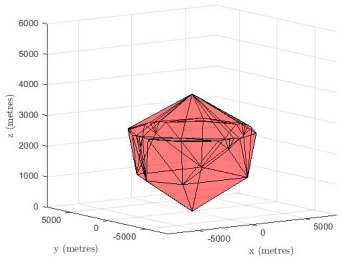	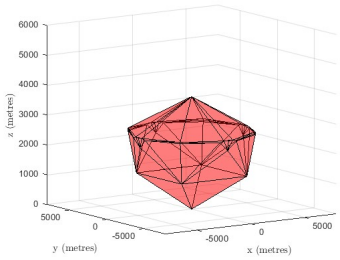
$D = 24$	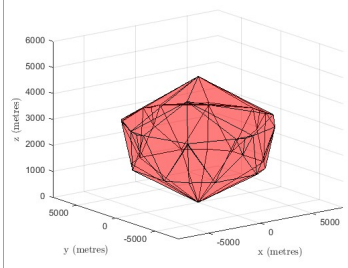	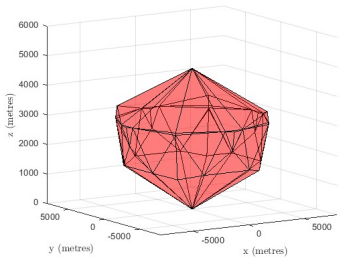	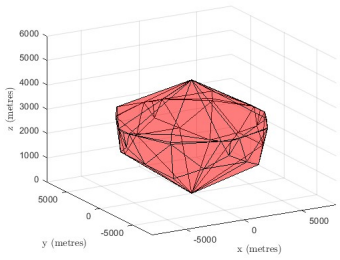
$D = 28$	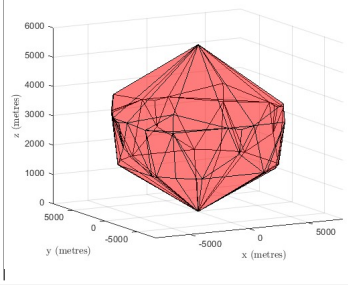	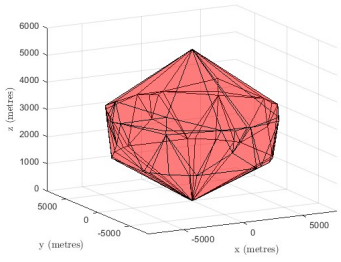	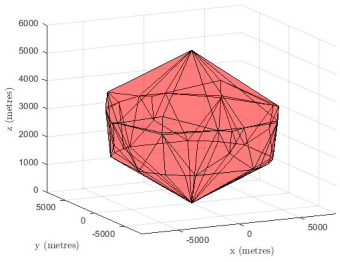

Table 1 Subset of 2-D array of D-step controllable sets parameterized by mass and divert length and projected onto position dimensions.

- **Hazards and topographic favorability:** Due to the highly uneven topography of the lunar south pole, hazard detection via a topological mapping sensor such as a LiDAR sensor is essential for real-time target selection

during the landing phase. This attribute is dynamic, due to greater imaging resolution as the spacecraft gets closer to the surface. Areas receiving sunlight are given a higher priority.

- **Scientific output potential:** Depending on the mission requirements, it may be favorable to land at or near a shadowed crater that may contain water ice. This attribute is assigned in tandem with the hazard attribute, as there may exist an overlap in hazardous regions with high scientific output potential, e.g. highly craterized permanently shadowed regions that may contain water ice.

Algorithm 1 depicts the computation of the best divert-feasible set. The scoring metric J incorporates the above mentioned attributes of each divert-feasible site. In this work, we provide randomized values in the range $[0, 1]$ to Algorithm 1, to simulate these attributes. It may be assumed that locations of high scientific interest are known a-priori, with scores for each site provided to the guidance algorithm during the mission design phase.

Algorithm 1 Computation of the best divert-feasible set

Input: Set of targets $\mathcal{L}$, collection of D-step controllable sets $\mathcal{K}(m, D)$ for various initial mass m for every $(m, D) \in \mathcal{M} \times \mathcal{D}$, scoring metric $J : \mathcal{L} \times \mathcal{M} \times \mathcal{D} \to \mathbb{R}$, the state at which hazard is detected ξ

Output: Best divert-feasible set $\mathcal{B}(\ell^*, m^*, D^*)$ and the best divert landing site ℓ^*

Compute the set of relevant divert feasible sets $\mathscr{B} = \{(\ell, m, D) : \xi \in \mathcal{B}(\ell, m, D)\}$ that include the state ξ for each divert landing site $\ell \in \mathcal{L}$, initial mass before divert $m \in \mathcal{M}$, and divert trajectory length $D \in \mathcal{D}$

Compute $\ell^*, m^*, D^* \leftarrow \arg\min_{(\ell,m,D)\in\mathscr{B}} J(\ell, m, D)$

Algorithm 2 Trajectory generation for lunar landing with feasible divert

Input: Initial position r_0, initial velocity v_0, initial mass $m(0)$, time step for nominal trajectory N, discrete time step to use in divert $\Delta t'$, altitude at which hazards are observable H, set of discrete mass of lunar lander to consider for divert computation $\mathcal{M}$, set of divert trajectory lengths to consider for divert computation $\mathcal{D}$, set of targets $\mathcal{L}$, scoring function J

Output: Trajectory $\{\xi_k\}_{k\geq 0}$ to land at origin, or divert safely in the event of detection of a hazard

Offline:

Compute $\mathcal{K}(m, D)$ for $m \in \mathcal{M}$ and $D \in \mathcal{D}$

Online:

Solve for optimal control $\{\mu_k^*\}_{k=0}^N$ for nominal landing using golden search and (7)
Initialize $k \leftarrow 0$, $\xi_0 \leftarrow [r_0, v_0, \ln(m(0))]$, $\tau \leftarrow 0$
while $k \leq N$ **do**
    if Altitude $r_{3,k} \leq H$ and a hazard is detected at the current state ξ_k **then**
        Use Algorithm 1 to obtain the best divert-feasible set $\mathcal{B}(\ell^*, m^*, D^*)$ and the best divert landing site $\ell^* \in \mathcal{L}$ for some initial mass before divert $m^* \leq \exp(\xi_{7,k})$, and some divert trajectory length $D^* \in \mathbb{N}$
        Solve (7) for $N = D^*$, initial state $(\xi_k - [\ell^*, 0, 0])$, and $t_f = N\Delta t'$ to compute the control for divert $\{\eta_k^*\}_{k=0}^N$
        Overwrite $\mu_{k+i}^* = \eta_i^*$ for all $i \in \mathbb{N}_{[0,D^*]}$
        Store the instant of divert as $\tau \leftarrow k$
        Reset $k \leftarrow 0$, and $N \leftarrow D^*$
    end if
    Apply control $\mu_{k+\tau}^*$ to obtain $\xi_{k+\tau+1}$
    Increment $k \leftarrow k + 1$
end while

The trajectory generation algorithm for lunar landing with feasible divert is detailed in Algorithm 2, which solves Problem 1.

V. Results

The convex optimization process provides the fuel-optimal trajectory from a given initial state $x_0 \in \mathbb{R}^7 = [r_0; v_0; m(0)]^T$ to the final state $x_f = [r(t_f); v(t_f); m(t_f)]$, subject to the dynamics and constraints specified in the

previous section. The initial trajectory conditions for this study are

$$r_0 = [-20000; 30000; 40000]^T m,\ v_0 = [200; -10; -15]^T m/s,\ r(t_f) = [0; 0; 0]^T m,\ v(t_f) = [0; 0; 0]^T m/s,\ m(0) = 2500\ kg,$$
$$N = 100\ \theta = 25^\circ,\ I_{\text{sp}} = 225\ s,\ \gamma_{\text{gs}} = 15\,\text{deg} \quad (10)$$

Algorithm 2 solves Problem 1 from the initial condition described in (10) to the final rest condition at origin to obtain a nominal trajectory, depicted in Figure 2.

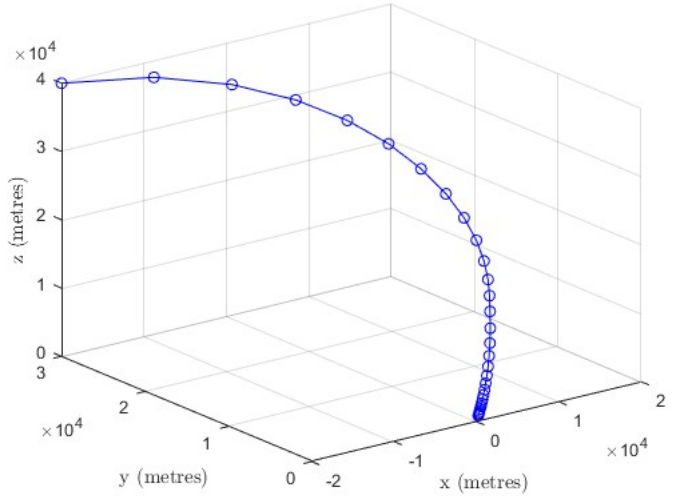

Fig. 2 Nominal lander trajectory

Figure 3 demonstrates the divert capability achieved through methods in this study. A divert trajectory is calculated to an alternate landing site $\ell = [-500; -457; 0]m$, with the divert maneuver initialized at the state $r = 1e03 \times [3.9902; 2.8307; 3.000]\ m, v = [-68.3959; -52.8986; -58.6963]\ m/s, m = 274.1473\ kg, t = 111.605\ s$. At an altitude $\leq$ 1500 meters, Algorithm 1 is invoked. The current state of the spacecraft is obtained, which is utilized

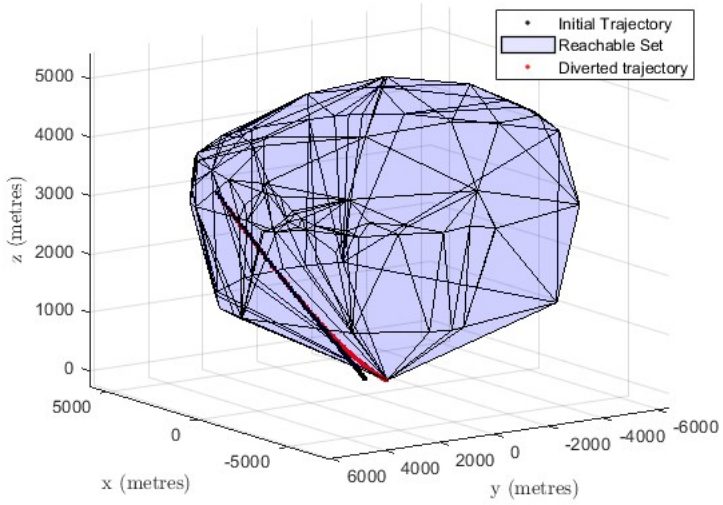

Fig. 3 Divert Trajectory

to select the appropriate controllable sets translated to the targets such that the current state lies within them. This

calculates the feasibility to the multiple alternate landing sites available to the spacecraft from the current state, and landing sites are prioritized. Figure 4 depicts the divert maneuver to a randomly selected trio of alternate landing sites, with the controllable sets corresponding to the mass of fuel m and divert length D at which the divert maneuver was initialized.

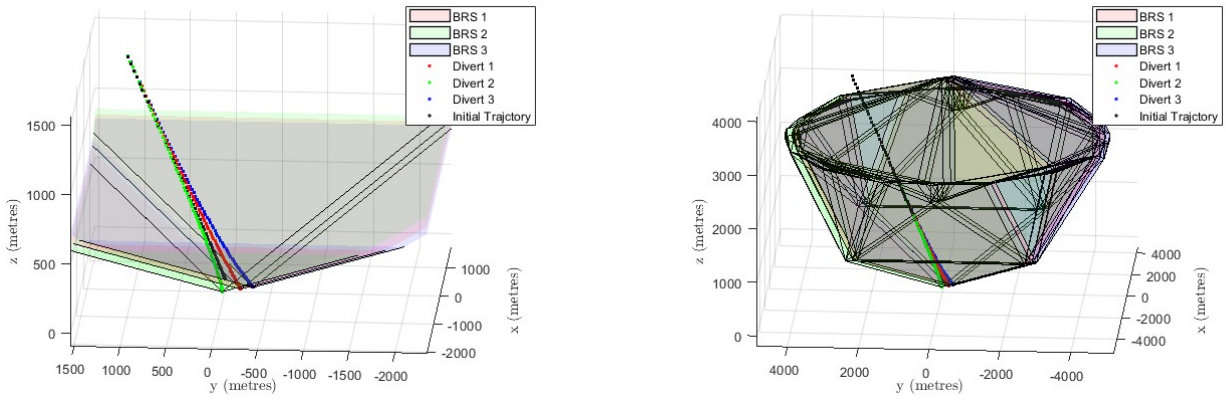

Fig. 4 Trajectories to divert-feasible sites within $1km^2$

Set S contains multiple divert-feasible landing targets, provided sufficient information about the current state and the landing sites are available. Although the simulation in Figure 4 demonstrates three targets selected within the primary landing zone of 1 km^2, diverts are possible to any target location whose divert-feasible set includes the current state, for fuel mass values not greater than the current fuel mass available to the lander. Figure 5 depicts two divert maneuvers from the state $r = 1e03 \times [2.0003; 1.3545; 1.4106]m, v = [-56.0274; -38.4224; -40.1378]m/s, m = 222.076kg$ to target sites of $\ell_1 = [-1030; 0; 0]m$ and $\ell_2 = [357; -1018; 0]m$ respectively. The two controllable sets depicted represent projections onto the positional dimenstions generated for $D = 23, m = 221kg$ (depicted in blue) and $D = 28, m = 190kg$ (depicted in red).

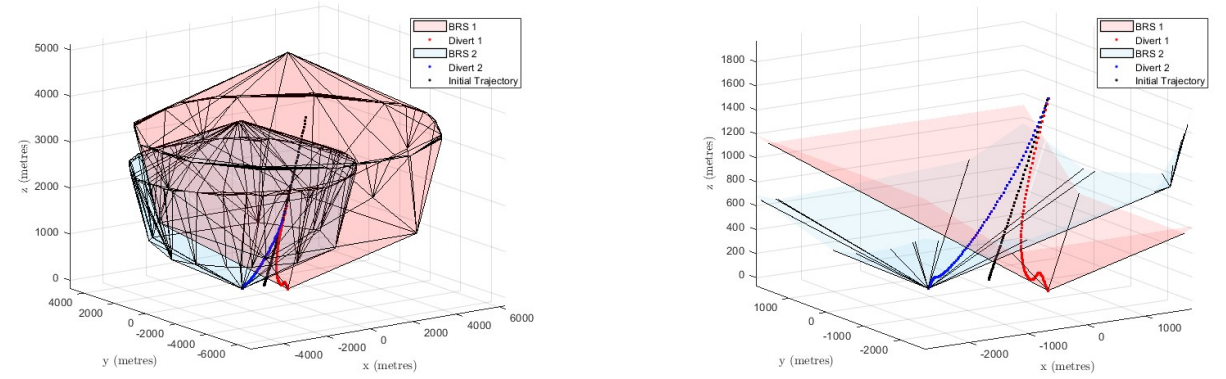

Fig. 5 Divert trajectories to distant targets

VI. Visualization & TRN

Preliminary work has been conducted to create a high-fidelity environment where the results of the optimized trajectory can be visualized. In addition, data obtained from the visualization environment is utilized to perform a basic version of terrain relative navigation (TRN), state estimation, and hazard detection. Simulink and the MATLAB UAV

Toolbox are utilized to visualize the results of the optimized trajectory. The fuel-optimal trajectory data obtained by solving problem (7) are provided to Simulink, which executes the dynamics in the visualization environment. The Simulink model is depicted in Figure 6.

The Simulation 3D UAV Vehicle block accepts the translational data obtained from problem (7) and simulates a UAV inside Unreal Engine. The mesh file for this UAV may be customized, and is provided a model of the Apollo 11 Lunar Module. The Simulation 3D Scene Configuration block interacts with the visualization environment of UE4.26, to which a custom scene of the lunar surface is provided. Two cameras are included in this model, utilizing the Simulation 3D Camera block. A Kalman Filter block has been implemented to provide state estimates using data obtained from the cameras, and a LiDAR block which performs hazard detection is also included in the model. Further details of these components are provided below. The custom MATLAB code blocks implement a variety of operations such as normalization and cross correlation of the images, used for position estimation from visual data.

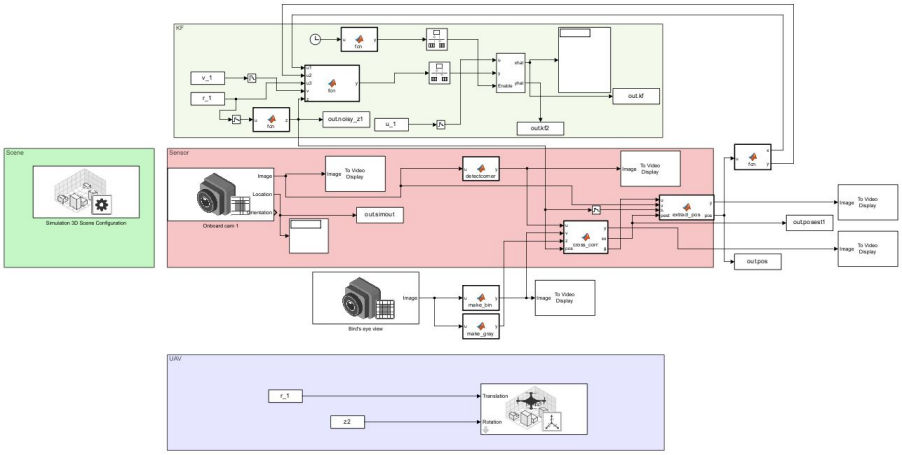

Fig. 6 Simulink model

A. Visualization Environment

Unreal Engine 4.26 has been utilized to visualize the lunar environment. Using publicly available high-resolution lunar terrain data captured by the Lunar Reconnaissance Orbiter (LRO) in the form of digital elevation maps (DEM), the topography of the lunar south pole can be rendered with high fidelity in UE4.26, as depicted in Figure 7. Due to the granularity and level of customization options available for scenes in UE4.26, the lighting at the south pole can be reproduced, allowing the permanently shadowed regions (PSR) of the lunar south pole to be modeled with a high degree of accuracy.

The fuel-optimal trajectory data in Simulink is visualized in the lunar south pole environment using UE4.26 as shown in Figure 8. In addition to visualization, the Simulink-UE connection allows for in-situ measurements during the trajectory, utilizing the Simulation 3D Camera modules in the UAV Toolbox. In this work, two camera models are implemented in the Simulink model: Camera 1 acts as an on-board camera facing the negative z direction, and Camera 2 which is stationary and acts as a bird's eye view camera. The bird's eye view camera acts as a reference map of the overall lunar south pole. This formulation ensures the lighting conditions in the reference map and the on-board camera are similar. The properties of the camera models are detailed in Table (2).

B. Localization and Terrain Relative Navigation

Terrain relative navigation involves the measurement of topographic features via sensors such as lidars and cameras, and comparing these measurements to a terrain map to estimate the position of the vehicle [21]. Utilizing the image output of the two cameras in the Simulink model, the position of the spacecraft with respect to the reference map of the south pole is obtained. First, a coarse position is obtained using normalized image correlation, following which, individual features in the two images are matched to obtain a refined position estimate.

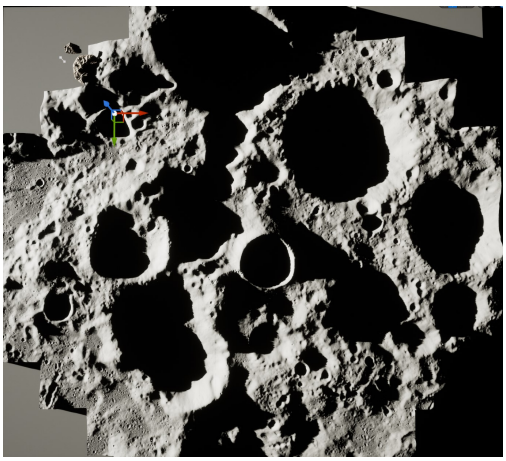

(a) 200 × 200 km landscape

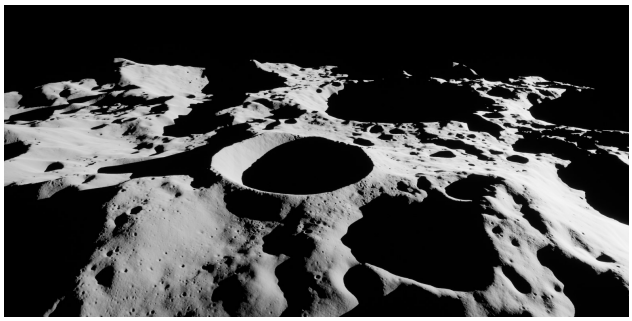

(b) Shackleton Crater (Center)

Fig. 7 Lunar south pole with PSRs modeled in UE4.26

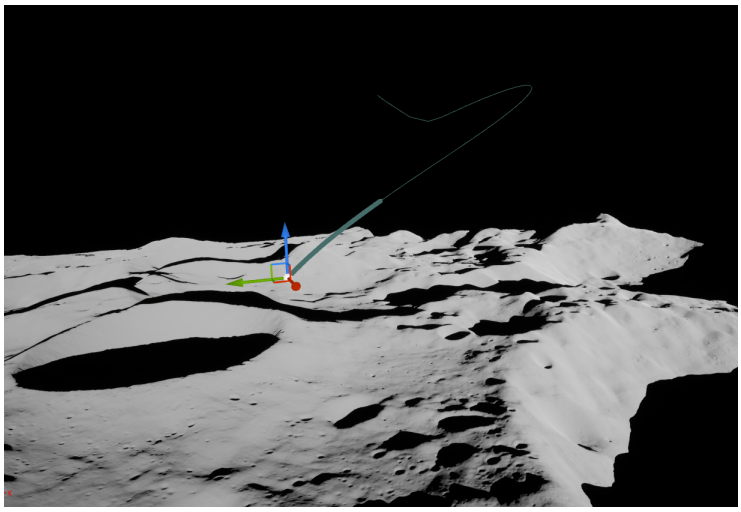

Fig. 8 Fuel-optimal trajectory visualized in UE4.26

Table 2 Simulink Camera Properties

Properties	Camera 1	Camera 2
Position (m)	Spacecraft	$[0; 0; 100000]^T$
Relative rotation (degrees)	$[0, 90, 0]$	$[0, 90, 0]$
Focal length (pixels)	[1109, 1109]	[1109, 1109]
Image size (pixels)	[1516, 1516]	[1389, 1656]
FOV (degrees)	90°	90°

1. Coarse position estimation

Normalized 2D image correlation [22] is utilized to obtain a coarse estimate of the lander's position within the reference map. We consider the image output of the on-board camera (Camera 1) as a template, and compare it to the image output of the bird's eye view camera (Camera 2) to obtain the best correlation coefficient between the two. The

image from Camera 1 is resized in accordance with the altitude such that the image footprint d^2 remains constant, where

$$d = 2\hat{r}_z tan(\frac{\theta}{2}), \tag{11}$$

θ is the field of view of the camera, and $\hat{r}_z$ is a noisy estimate of the altitude. The correlation coefficient is given by

$$\Gamma(u,v) = \frac{\sum_{i,j}[f(i,j) - \bar{f}_{u,v}][t(i-u, j-v) - \bar{t}]}{\sqrt{\sum_{i,j}[f(i,j) - \bar{f}_{u,v}]^2 \sum_{i,j}[t(i-u, j-v) - \bar{t}]^2}}, \tag{12}$$

where f is the image (Camera 2) with coordinates (i, j), t is the template (Camera 1) with coordinates (u, v) that correspond to the location in (i, j) space where the template is placed, $\bar{t}$ is the mean of the template, and $\bar{f}_{u,v}$ is the mean of $f(i, j)$ in the region under the template [23]. The argmax of (12) is used to construct a bounding box in the image (Camera 2) of equal size to the template obtained from the on-board camera, as shown in Figure 9. The center of the bounding box gives the coarse position estimate in (i, j) space.

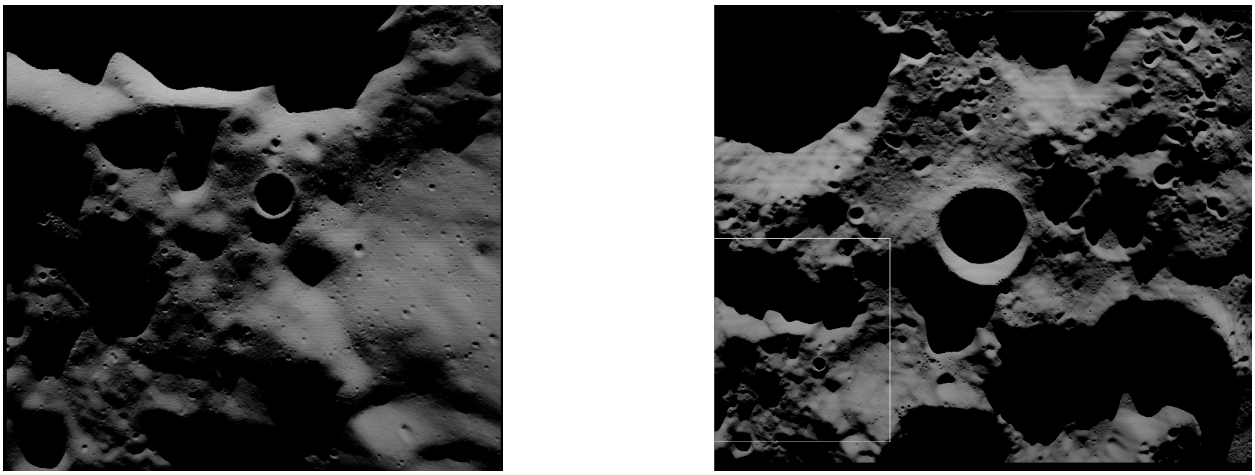

(a) On-board camera view **(b) Reference map with bounding box**

Fig. 9 Coarse position estimation

2. Feature Matching

Consider the center of the image obtained from the on-board camera (Camera 1) to be the true position. The normalized image correlation provides a coarse position estimation via a bounding box that may or may not have it's center aligned with the center of the image obtained from Camera 1. This discrepancy may lead to position estimation errors that can correspond to 10s of kilometers depending on the altitude of the spacecraft. To refine this estimate, individual features inside the bounding box are matched with the corresponding features in the image obtained from the on-board camera.

The speeded-up robust features (SURF) algorithm is utilized to detect features in the two images. SURF utilizes Hessian matrices to identify the local change around a point and points of interest are chosen based on the determinant values of the Hessain matrices [24]. Descriptors are then constructed which describe every point of interest identified in the image. By comparing descriptors in two separate images, matching pairs can be extracted which describe the same point of interest. The distance offset between the same set of features is then extrapolated, facilitated by the prior knowledge of the image resolutions and noisy altitude data. The image obtained from Camera 1 is resized to be the same size as the bounding box in pixels, for best results. An example of feature matching is depicted in Figure 10. The blue circles indicate features detected from the on-board camera image and the red circles represent the same features, detected inside the bounding box of position estimate. For a feature f_c detected in the image obtained from the on-board camera and correlated to a feature f_b obtained from the bounding box, the Euclidean distance between the (x, y) coordinates of the feature is calculated. The average distance between the strongest subset of such features detected in both images (x_{avg}, y_{avg}) is then calculated, and the coarse position estimate obtained from the center of the bounding box is adjusted by shifting it by the average distance offset.

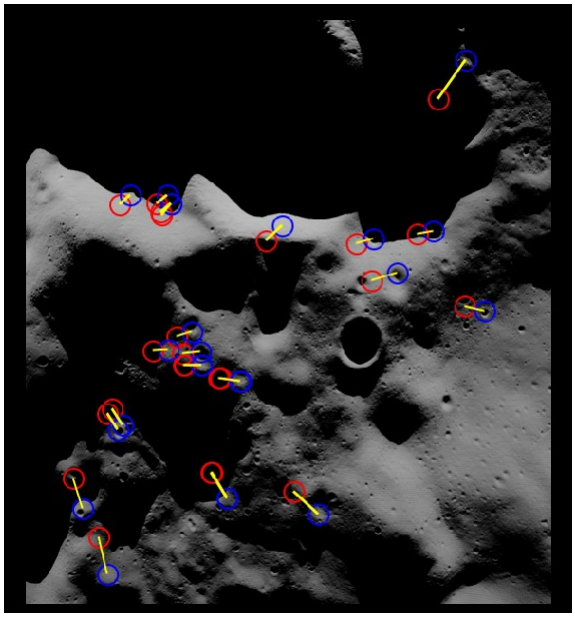

Fig. 10 Feature matching

C. State Estimation

Utilizing the position estimation data obtained from the feature matching process, a Kalman filter has been implemented to estimate the states of the spacecraft. The measurements to the filter are the position estimate data in $[r_x, r_y]$ and noisy altitude data r_z. The process noise covariance and measurement noise covariance are given by $700 \times I_{6\times6}$ and $15000^2 \times I_{3\times3}$, respectively, based on a coarse tuning of the filter. The filter is initialized at an initial state different from the actual initial state, and the measurements are used until the lander reaches an altitude of 15km above the surface ($\sim 70\%$ of the trajectory). This measurement cutoff is implemented due to Camera 1 not being able to image sufficiently large areas on the surface to correlate with the reference map as the spacecraft lowers in altitude and coarse localization fails. As seen in Figure 11, once the coarse localization fails the lander relies on dead reckoning. The results in Figure 11 reflect the usage of visual data alone to perform TRN in $[r_x, r_y]$, and exhibit deviations from the true states. State of the art TRN techniques for lunar landings utilize a location coordinate dataset of known features such as craters, resulting in better state estimates [25].

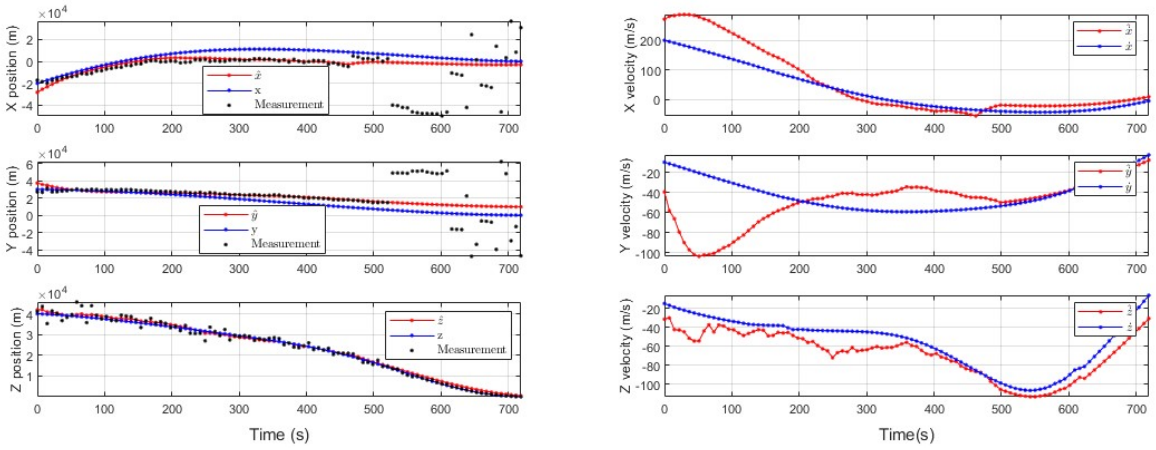

(a) Position **(b) Velocity**

Fig. 11 Estimted states, true states, and measurements

D. Hazard Detection

This section details an example implementation of a hazard detection system that utilizes a simulated LiDAR sensor. Through the 3-dimensional imaging functionality of the LiDAR sensor, an elevation map of the surface is obtained, which is further analyzed to detect and classify areas on the surface as viable or non-viable for a safe landing. The visualization environment in UE4.26 is utilized to simulate obstacles at the primary landing site, which are then detected by the LiDAR sensor incorporated in the Simulink model. Figure 12 depicts the obstacles as visualized in UE4.26 and the corresponding site as captured by the LiDAR sensor.

A simple morphological filter (SMRF) [26] algorithm is utilized to classify the point cloud data into ground and non-ground points via the MATLAB function $segmentgroundSMRF$. The LiDAR sensor has a 90° field in both the vertical and horizontal directions and has a range of 500 meters, which is sufficient for surveying a footprint area of $1km^2$ at an altitude of 500m. The footprint of the lander is assumed to be a circle with radius of 5 meters, which includes the actual dimensions of the lander and a buffer zone which may be utilized for auxiliary activities such as the deployment of rovers. Figure 13 depicts the classification of ground points from an altitude of $\sim$ 250 meters, with an elevation threshold of 5.5. The obstacles at the primary landing site can be seen on the top-right hand side of the image, as detected by the LiDAR and classified as obstacles.

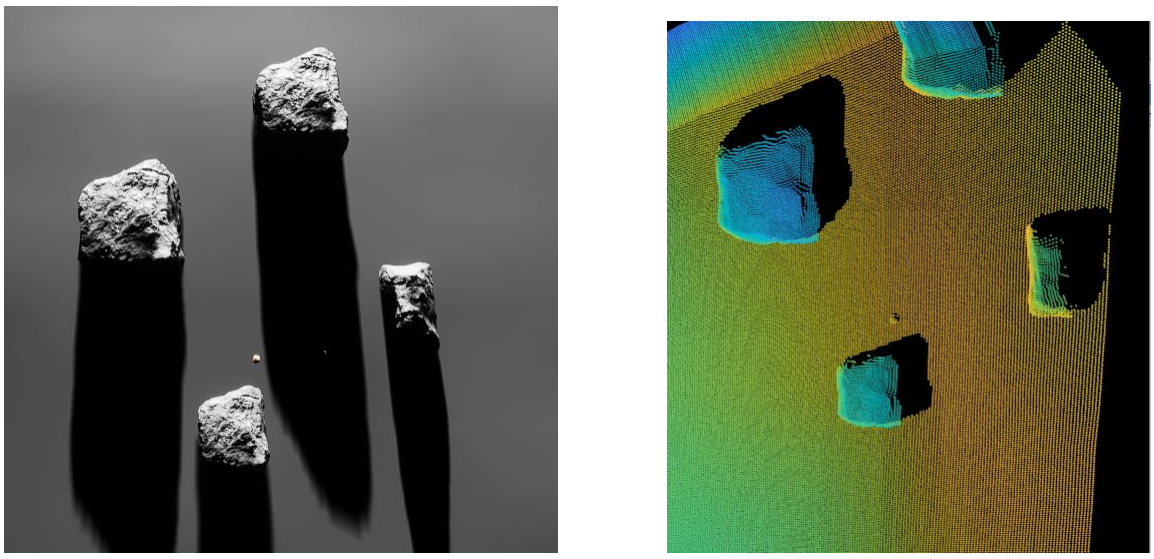

(a) UE4.26 **(b) LiDAR output**

Fig. 12 Hazards at the primary landing site, UE4.26 and LiDAR point cloud

VII. Conclusion and Future Work

This work establishes a convex optimization based method to ensure successful landing of a lunar lander under given state and path constraints, while maintaining the ability to divert to alternate landing sites. Divert ability is achieved through the use of controllable sets that characterize a set of initial conditions from which a divert target is viable. The best divert site is selected by quantifying fuel usage, time required to reach, and a scoring metric that represents site hazards and the scientific output potential. A visualization environment was developed, where the fuel-optimal trajectory was visualized. Visual data from the visualization environment was utilized in preliminary work to perform state estimation and hazard detection.

Future work will aim to improve the localization and TRN capabilities, incorporating location data of known features and landmarks on the lunar surface. Additionally, the state information obtained from the TRN implementation will be utilized in divert site selection. Finally, the controllable sets will be constructed with state uncertainties to improve robustness and enable closed-loop autonomous landing trajectory generation based on TRN state estimates.

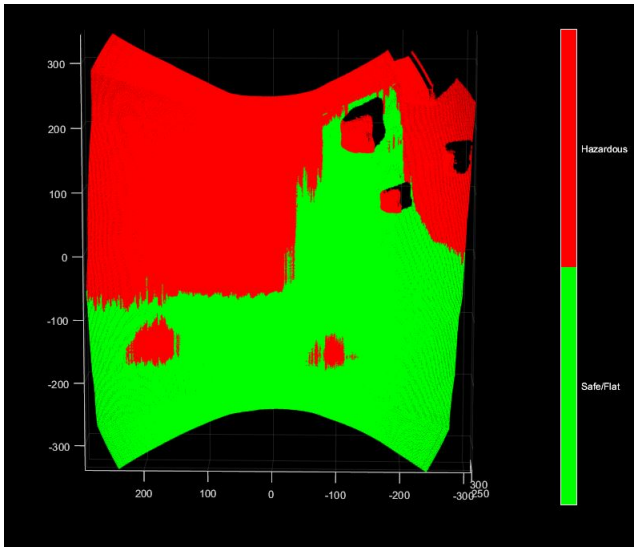

Fig. 13 Ground classification

References

[1] Anand, M., "Lunar water: a brief review," *Earth, Moon, and Planets*, Vol. 107, 2010, pp. 65–73.

[2] Smith, M., Craig, D., Herrmann, N., Mahoney, E., Krezel, J., McIntyre, N., and Goodliff, K., "The artemis program: An overview of nasa's activities to return humans to the moon," *2020 IEEE Aerospace Conference*, IEEE, 2020, pp. 1–10.

[3] Hernando-Ayuso, J., Ozawa, Y., Takahashi, S., Campagnola, S., Ikenaga, T., Yamaguchi, T., Yam, C., Sarli, B., and Hashimoto, T., "Trajectory design for the JAXA moon nano-lander OMOTENASHI," 2017.

[4] Padma, T., et al., "India gears up for second Moon mission," *Nature*, Vol. 550, No. 7677, 2017, pp. 440–440.

[5] Calzada-Diaz, A., Acierno, K., Rasera, J., and Lamamy, J.-A., "ispace's Polar Ice Explorer: Commerically Exploring the Poles of the Moon," *New Views of the Moon 2-Asia*, Vol. 2070, 2018, p. 6010.

[6] Quaide, W., and Oberbeck, V., "Geology of the Apollo landing sites," *Earth-Science Reviews*, Vol. 5, No. 4, 1969, pp. 255–278.

[7] Klumpp, A. R., "Apollo lunar descent guidance," *Automatica*, Vol. 10, No. 2, 1974, pp. 133–146.

[8] Epp, C. D., Robertson, E. A., and Brady, T., "Autonomous landing and hazard avoidance technology (ALHAT)," *2008 IEEE Aerospace Conference*, IEEE, 2008, pp. 1–7.

[9] Nelessen, A., Sackier, C., Clark, I., Brugarolas, P., Villar, G., Chen, A., Stehura, A., Otero, R., Stilley, E., Way, D., et al., "Mars 2020 entry, descent, and landing system overview," *2019 IEEE Aerospace Conference*, IEEE, 2019, pp. 1–20.

[10] Scharf, D. P., Açıkmeşe, B., Dueri, D., Benito, J., and Casoliva, J., "Implementation and Experimental Demonstration of Onboard Powered-Descent Guidance," *Journal of Guidance, Control, and Dynamics*, Vol. 40, No. 2, 2017, pp. 213–229. https://doi.org/10.2514/1.G000399, URL https://doi.org/10.2514/1.G000399.

[11] Ueda, S., Ito, T., and Sakai, S.-i., "A study on guidance technique for precise lunar landing," *Proceedings of 31st ISTS*, 2017.

[12] Iiyama, K., Tomita, K., Jagatia, B. A., Nakagawa, T., and Ho, K., "Deep reinforcement learning for safe landing site selection with concurrent consideration of divert maneuvers," *arXiv preprint arXiv:2102.12432*, 2021.

[13] Dang, Q., Gui, H., Liu, K., and Zhu, B., "Relaxed-constraint pinpoint lunar landing using geometric mechanics and model predictive control," *Journal of Guidance, Control, and Dynamics*, Vol. 43, No. 9, 2020, pp. 1617–1630.

[14] Lee, U., and Mesbahi, M., "Constrained Autonomous Precision Landing via Dual Quaternions and Model Predictive Control," *Journal of Guidance Control and Dynamics*, Vol. 40, 2017, pp. 292–308.

[15] Cohanim, B. E., and Collins, B. K., "Landing point designation algorithm for lunar landing," *Journal of Spacecraft and Rockets*, Vol. 46, No. 4, 2009, pp. 858–864.

[16] Acikmese, B., and Ploen, S. R., "Convex programming approach to powered descent guidance for mars landing," *Journal of Guidance, Control, and Dynamics*, Vol. 30, No. 5, 2007, pp. 1353–1366.

[17] Eren, U., Dueri, D., and Açıkmeşe, B., "Constrained reachability and controllability sets for planetary precision landing via convex optimization," *Journal of Guidance, Control, and Dynamics*, Vol. 38, No. 11, 2015, pp. 2067–2083.

[18] Blackmore, L., Açikmeşe, B., and Scharf, D. P., "Minimum-landing-error powered-descent guidance for Mars landing using convex optimization," *Journal of guidance, control, and dynamics*, Vol. 33, No. 4, 2010, pp. 1161–1171.

[19] Dueri, D., Zhang, J., and Açikmese, B., "Automated custom code generation for embedded, real-time second order cone programming," *IFAC Proceedings Volumes*, Vol. 47, No. 3, 2014, pp. 1605–1612.

[20] Borrelli, F., Bemporad, A., and Morari, M., *Predictive control for linear and hybrid systems*, Cambridge University Press, 2017.

[21] Johnson, A. E., and Montgomery, J. F., "Overview of terrain relative navigation approaches for precise lunar landing," *2008 IEEE Aerospace Conference*, IEEE, 2008, pp. 1–10.

[22] Yoo, J.-C., and Han, T. H., "Fast normalized cross-correlation," *Circuits, systems and signal processing*, Vol. 28, 2009, pp. 819–843.

[23] Lewis, J., "Fast Normalized Cross-Correlation," *Ind. Light Magic*, Vol. 10, 2001.

[24] Bay, H., Tuytelaars, T., and Van Gool, L., "Surf: Speeded up robust features," *Lecture notes in computer science*, Vol. 3951, 2006, pp. 404–417.

[25] Downes, L. M., Steiner, T. J., and How, J. P., "Lunar terrain relative navigation using a convolutional neural network for visual crater detection," *2020 American Control Conference (ACC)*, IEEE, 2020, pp. 4448–4453.

[26] Pingel, T. J., Clarke, K. C., and McBride, W. A., "An improved simple morphological filter for the terrain classification of airborne LIDAR data," *ISPRS Journal of Photogrammetry and Remote Sensing*, Vol. 77, 2013, pp. 21–30. https://doi.org/https://doi.org/10.1016/j.isprsjprs.2012.12.002, URL https://www.sciencedirect.com/science/article/pii/S0924271613000026.